

Detailed simulation and characterization of double paraboloidal monocapillary for laboratory x-ray sources

Shang-Kun Shao(邵尚坤), Tian-Yu Yuan(袁天语), Cheng-Bo Li(李成波), Xing-Yi Wang(王兴艺), Lu Hua(华陆), Yu-Chuan Zhong(钟玉川), Jin-Yue Hu(胡锦玥), Meng-Fang Chen(陈盟方), Xue-Peng Sun(孙学鹏), and Tian-Xi Sun(孙天希)

Citation: Chin. Phys. B, 2025, 34 (**12**): 124101. DOI: 10.1088/1674-1056/addcc3
http://cpb.iphy.ac.cn; http://iopscience.iop.org/cpb

What follows is a list of articles you may be interested in

Intensity correlation properties of x-ray beams split with Laue diffraction

Chang-Zhe Zhao(赵昌哲), Shang-Yu Si(司尚禹), Hai-Peng Zhang(张海鹏), Lian Xue(薛莲), Zhong-Liang Li(李中亮), and Ti-Qiao Xiao(肖体乔)
Chin. Phys. B, 2024, 33 (**1**): 014102. DOI: 10.1088/1674-1056/acf206

Attosecond laser station

Hao Teng(滕浩), Xin-Kui He(贺新奎), Kun Zhao(赵昆), Zhi-Yi Wei(魏志义)
Chin. Phys. B, 2018, 27 (**7**): 074203. DOI: 10.1088/1674-1056/27/7/074203

Property of slice square polycapillary x-ray optics

Shi-Qi Peng(彭诗棋), Zhi-Guo Liu(刘志国), Tian-Xi Sun(孙天希), Kai Wang(王锴), Long-Tao Yi(易龙涛), Kui Yang(杨魁), Man Chen(陈曼), Jin-Bang Wang(王金榜)
Chin. Phys. B, 2016, 25 (**2**): 024102. DOI: 10.1088/1674-1056/25/2/024102

X-ray communication based simultaneous communication and ranging

Song Shi-Bin (宋诗斌), Xu Lu-Ping (许录平), Zhang Hua (张华), Gao Na (高娜)
Chin. Phys. B, 2015, 24 (**9**): 094215. DOI: 10.1088/1674-1056/24/9/094215

Polycapillary X-ray lens for secondary focusing Beijing synchrotron radiation source

Li Yu-De (李玉德), Lin Xiao-Yan (林晓燕), Liu Shi-Gang (刘世岗), He Jin-Long (何金龙), Guo Fei (郭非), Sun Tian-Xi (孙天希), Liu Peng (刘鹏)
Chin. Phys. B, 2013, 22 (**4**): 044103. DOI: 10.1088/1674-1056/22/4/044103

Detailed simulation and characterization of double paraboloidal monocapillary for laboratory x-ray sources

Shang-Kun Shao(邵尚坤)[1,2], Tian-Yu Yuan(袁天语)[1,2], Cheng-Bo Li(李成波)[1], Xing-Yi Wang(王兴艺)[3], Lu Hua(华陆)[1,2], Yu-Chuan Zhong(钟玉川)[1,2], Jin-Yue Hu(胡锦玥)[1,2], Meng-Fang Chen(陈盟方)[1,2], Xue-Peng Sun(孙学鹏)[1,2,†], and Tian-Xi Sun(孙天希)[1,2,‡]

[1] *Institute of Radiation Technology, Beijing Academy of Science and Technology, Beijing* 100875, *China*
[2] *Key Laboratory of Beam Technology of the Ministry of Education, School of Physics and Astronomy, Beijing Normal University, Beijing* 100875, *China*
[3] *School of Physics and Engineering, Henan University of Science and Technology, Luoyang* 471023, *China*

(Received 10 April 2025; revised manuscript received 12 May 2025; accepted manuscript online 23 May 2025)

A double-parabola monocapillary (DPM) was designed for laboratory x-ray sources, and its performance was evaluated through numerical simulations and experimental validation. A surface shape error model was developed to characterize the DPM surface profile, and ray-tracing methods were used to simulate key properties such as focal spot size, divergence, and transmission efficiency. The simulation results closely matched experimental measurements, validating the proposed model. This surface shape error simulation provides an efficient method for evaluating the impact of slope errors on DPM performance, offering insights for optimal design and precision manufacturing.

Keywords: double paraboloidal monocapillary, capillary x-ray optics, laboratory x-ray source

PACS: 41.50.+h, 42.55.Vc, 41.50.+h, 07.85.–m

DOI: 10.1088/1674-1056/addcc3 **CSTR:** 32038.14.CPB.addcc3

1. Introduction

Capillary x-ray optics is an important reflection-type x-ray optical device based on total external reflection of x-rays, including polycapillary x-ray optics and monocapillary x-ray optics. Polycapillary x-ray optics, with the gain of up to 1000 in power density and focal spot size of tens of microns, is widely used in some applications, such as micro x-ray fluorescence,[1] micro x-ray diffraction,[2] micro extended x-ray absorption fine structure.[3] Compared with polycapillary x-ray optics, the monocapillary x-ray optics can provide a micro-x-ray beam with smaller focal spot size (hundreds of micrometers to tens of nanometers) and divergence angle, and it has been used in full-field transmission x-ray microscopy,[4] energy-dispersive small-angle x-ray scattering,[5] and total reflection x-ray fluorescence technologies.[6,7]

Monocapillaries can be divided into multi-bounce capillaries (MBC) and single-bounce capillaries (SBC), as shown in Fig. 1. The inner surface of MBC is usually fabricated as a tapered surface to reflect x-rays multiple times from a larger entrance to a smaller exit, and the reflection angle increases with the number of reflections, as shown in Fig. 1(a). The focal spot size of MBC depends on the exit aperture and is generally slightly smaller than the exit aperture.[8–10] This type of monocapillary has the disadvantages of short working distance, uncontrollable divergence, low transmission efficiency and small receiving solid angle, which restrict its application field. SBCs can be divided into single-bounce ellipsoidal capillaries (SBEC) and single-bounce paraboloidal capillaries (SBPC), which have the advantages of larger working distance, controllable divergence and high transmission efficiency.[11] SBEC is used to collect x-ray radiation and focus it into a focal spot and is the most commonly used type of SBC. Figure 1(b) shows the SBEC-1 type with an input focal distance f_1 smaller than the major semi-axis. The length of the SBEC-1 type is generally larger, and its inner diameter first increases and then decreases along the y axis, which makes this SBEC-1 difficult to manufacture. Figure 1(c) shows the SBEC-2 type with a shorter length, which is easier to manufacture than the SBEC-1 type. The input focal distance f_1 of SBEC-2 type is usually greater than the major semi-axis, which results in a smaller receiving solid angle. Therefore, SBECs were usually used in some applications based on synchrotron radiation x-ray sources, such as full-field transmission x-ray microscopy,[4] micro small-angle x-ray scattering,[12] micro x-ray fluorescence,[13] micro x-ray diffraction,[14] micro extended x-ray absorption fine structure,[15] and confocal three-dimensional micro x-ray microscopy.[16]

The double paraboloidal monocapillary (DPM) is an assembled x-ray optics with two shorter SBPCs that are easier to fabricate than the SBEC-1 type, as shown in Fig. 1(d). The x-ray beam can be bounced twice to the focal spot of DPM, and DPM also has a fixed input focal distance f_1 and output focal

†Corresponding author. E-mail: sunxuepeng@brc.ac.cn
‡Corresponding author. E-mail: stx@bnu.edu.cn

© 2025 Chinese Physical Society and IOP Publishing Ltd. All rights, including for text and data mining, AI training, and similar technologies, are reserved.

distance f_2 like SBEC. Therefore, compared with MBC, DPM can also have the advantages of larger working distance, controllable divergence and high transmission efficiency. Furthermore, the input focal distance f_1 of the DPM can be designed to be smaller than that of the SBEC-2 type, so the receiving solid angle of the DPM can be larger than that of the SBEC-2 type, which increases the brightness of the x-ray beam at the focal spot. In particular, DPM has a great application prospect for full-field transmission x-ray microscopy based on laboratory x-ray sources. Compared with the SBEC, it can provide a higher-brightness x-ray illumination beam that can match the zone plate.

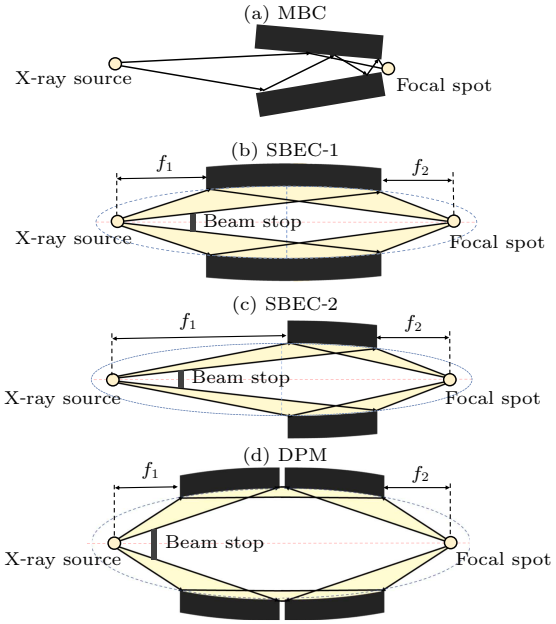


Fig. 1. Sketches of monoapillary x-ray optics reflecting x-rays. The x-ray beam is reflected twice on the inner surface of DPM.

In 2001 and 2006, Huang *et al*. used a geometric optics-based numerical method to simulate the focal spot size and gain of an SBEC, discussing the slope error, characterization, and theoretical limits of the SBEC.[11,17] In 2010, Lin *et al*. developed a simulation program for the SBEC using MATLAB, providing effective guidance for the manufacturing of the SBEC.[18] However, these simulations did not incorporate actual surface shape errors into the model, nor did they consider factors like roughness and air absorption attenuation, which affect SBEC performance.

In 1988, the group of Fiedorowicz from Poland successfully used the replica technology based on galvanoplastics to manufacture a double paraboloidal optics with an aperture of the order of centimeters for soft x-ray microscopy in nuclear fusion experiments.[19] The drawing tower method is a relatively simple way to manufacture glass monocapillary with apertures of a few microns to a few millimeters.[20] We manufactured a glass DPM with millimeter-scale aperture for laboratory hard x-ray sources by drawing tower method. In this paper, we present a slope error model and use ray-tracing methods to simulate key properties of DPM. The simulation incorporates the actual surface shape, considering factors such as surface roughness and air absorption attenuation. We compare the experimentally measured values of the focal spot size, divergence angle, and transmission efficiency of the DPM with the corresponding simulation results.

2. Model and simulation

The x-ray beam with a grazing incidence angle θ less than the critical angle θ_c of external total reflection can be totally reflected on the inner surface of the monocapillary. For DPM, incident x-ray beam from a laboratory x-ray source is first redirected into a quasi-parallel x-ray beam by an SBPC, which is then focused to a focal point by another SBPC, as shown in Fig. 1(c). Since DPM consists of two monocapillaries, it is only necessary to construct the model of SBPC.

2.1. Surface shape error model

We assume that the ideal centerline of monoapillary is the z-axis and ideal model of the SBPC can be built by

$$x^2+y^2=2pz, \tag{1}$$

where p is semi-latus rectum of paraboloid.

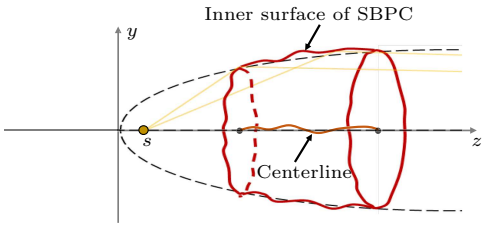


Fig. 2. Schematic diagram of an SBPC with surface shape error.

The surface shape error of inner surface of monoapillary is mainly the error of the straight line (centerline of monoapillary) and the error of the cross-sectional circle,[4] as shown in Fig. 2. In practice, monoapillary has a good average roundness of crosssection (generally greater than 0.95). Roundness is 1 for a perfect circular section of the monoapillary and goes down as far as 0 for a highly non-circular shape, the detailed explanation of roundness is given in Ref. [21]. The cross-sections of a large number of monocapillaries were measured with an optical microscope, it was found that the cross-sections of monocapillaries were basically elliptical and could generally be fitted by ellipse. Therefore, we assume that the cross-section of SBPC is an ellipse, the ideal centerline of monoapillary is the z-axis, and the centerline errors along the x-axis and y-axis are $d_x(z)$ and $d_y(z)$, respectively. The inner surface of SBPC model with the surface shape error can be built by

$$\frac{(x-d_x(z))^2}{(\sqrt{2pz}+\delta_a(z))^2}+\frac{(y-d_y(z))^2}{(\sqrt{2pz}+\delta_c(z))^2}=1, \tag{2}$$

where the major semi-axis of the elliptical cross-section is $\sqrt{2pz}+\delta_a(z)$, the minor semi-axis is $\sqrt{2pz}+\delta_b(z)$.

To obtain the centerline errors $d_x(z)$, $d_y(z)$, and semi-axis errors of the elliptical cross-section $\delta_a(z)$, $\delta_b(z)$ for the simulation, a digital micrometer device was used to measure the outer diameter data of the SBPC. A set of data was measured by moving a digital micrometer device along the z-axis, as shown in Fig. 3. After completing one set of data measurement, the SBPC was rotated by 10° to measure the next set of data until 36 sets of data were obtained. According to the constant ratio of inner and outer diameters of SBPC, the inner surface profile of SBPC could be calculated from the outer wall data. And, the centerline errors and semi-axis errors of the elliptical cross-section could be calculated from inner surface profile of SBPC. Details were given in Ref. [21]. Since it is difficult to find suitable function to fit such complex centerline errors and semi-axis errors. A spline interpolation method was used to obtain the centerline and semi-axis errors for the simulation.

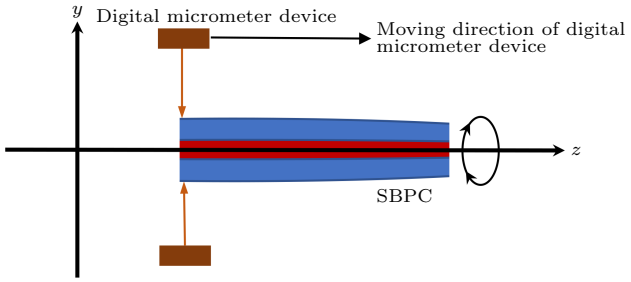


Fig. 3. Schematic diagram of digital micrometer device.

2.2. Simulation

To simulate the properties of a DPM, this research used ray-tracing method. As shown in Fig. 4, an x-ray beam from the x-ray laboratory source intersects the inner surface of the monocapillary at point A. The glancing incident angle can be expressed as

$$\theta = \sin^{-1}(\boldsymbol{n} \cdot \boldsymbol{u}), \tag{3}$$

where $\boldsymbol{n}$ is the outer normal unit vector for the inner surface of monocapillary, and $\boldsymbol{u}$ is the unit vector in the directions of the incident beam.

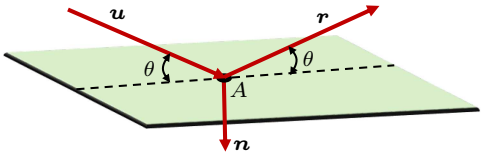


Fig. 4. Schematic diagram of the ray-tracing.

If the glancing incident angle θ is less than the critical angle θ_c of total reflection, the reflectivity R_0 can be described as[22]

$$R_0 = \frac{h-(\theta/\theta_c\sqrt{2(h-1)})}{h+(\theta/\theta_c\sqrt{2(h-1)})}, \tag{4}$$

where

$$h = \left(\frac{\theta}{\theta_c}\right)^2 + \left\{\left[\left(\frac{\theta}{\theta_c}\right)^2 - 1\right]^2 + \left(\frac{\beta}{\delta}\right)^2\right\}^{1/2}, \tag{5}$$

where δ and β are the real and imaginary parts of the refractive index of glass, respectively.

The reflectivity R for a surface with an RMS height of the roughness σ (in unit nm) can be described as[23,24]

$$R = R_0 \cdot \exp\left(-\frac{(4\pi\sigma\sin\theta)^2}{\lambda^2}\right). \tag{6}$$

The unit vector $\boldsymbol{r}$ in the directions of the reflected beam can be expressed as

$$\boldsymbol{r} = \boldsymbol{u} - 2\boldsymbol{n}\sin(\theta). \tag{7}$$

The unit vector $\boldsymbol{r}$ can be used as the incident vector for the next iteration calculation. This process is iterated until the x-ray beam exits the monocapillary or the glancing incident angle θ is greater than the critical angle θ_c of total reflection.

When DPM is used for hard x-ray focusing, it typically operates in air, where x-ray absorption by air becomes significant. For example, the x-ray intensity at 6 keV decreases by 28% after traveling 100 mm through air. Therefore, air absorption must be considered in DPM simulations. The intensity I of x-rays transmitted through a distance t of air can be expressed as

$$I = I_0 \mathrm{e}^{-\mu t}, \tag{8}$$

where I_0 is the initial intensity, μ is the linear attenuation coefficient of the air, which can be obtained from the NIST website.[25]

3. Experimental and method

There are generally two methods for characterizing DPM parameters based on the x-ray source. One method involves using a monochromatic synchrotron radiation source for more accurate measurements. The other is to use a polychromatic laboratory x-ray source for rapid measurements. Since synchrotron radiation facilities require advance scheduling and have limited operating times, making them inconvenient for timely feedback during DPM development. The synchrotron radiation-based characterization method is described in Ref. [26]. Therefore, this study uses a laboratory x-ray source, coupled with an energy-resolved silicon drift detector (SDD) and a CCD, to characterize the DPM.

Figure 5 shows the schematic diagram of the experimental setup. The x-ray source (Hamamatsu Photonics L9631) is a W (tungsten) x-ray generator with spot-size of 50 μm. In the experiment, the W target x-ray generator was operated at

30 kV and 600 μA. A pinhole and a beam stop, both 0.5 mm in diameter, were used to adjust the β_2 x-ray beam incident on DPM. The distances from the pinhole and beam stop to the source were 83 mm and 102 mm, respectively. Thus, the minimum incidence angle β_1, maximum incidence angle, and receiving solid angle Ω are 2.45 mrad, 3.00 mrad, and 1.04×10^{-5} sr, respectively. DPM can be adjusted by motorized x–y–z–θ_1–θ_2 stages. A SDD (AXAS-M, Amptek, Germany) with an energy resolution of < 139 eV at 5.9 keV was used to obtain the x-ray energy spectrum, and its sensitive area was 80 mm^2. A CCD detector (Hamamatsu C11440-22CU) with a 6.5-μm pixel size was used to obtain the images of the focal spot and far-field for DPM. Its optical magnification ratio is 0.5 with the actual resolution is 13 μm/pixel.

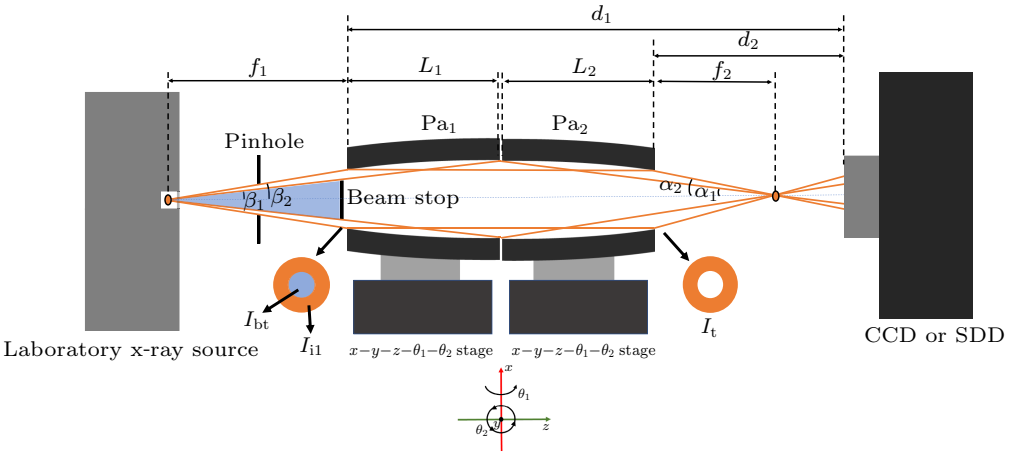


Fig. 5. Schematic diagram of the experimental setup.

To evaluate the quality of the DPM, we focus on such properties of the DPM, such as focal spot size, divergence angle, and transmission efficiency. As shown in Fig. 5, when the CCD was moved to a distance f_2 from the exit of DPM, the focal spot size of DPM can be measured by the CCD. Likewise, the divergence angle can be obtained by images from the CCD at different positions from the exit of DPM.

The transmission efficiency of a DPM can be expressed in two ways. One η_1 is defined as the ratio of the x-ray beam flux I_t transmitted through DPM to the x-ray beam flux I_{i1} entering DPM with beam stop and pinhole, and the other η_2 is the ratio of the x-ray beam flux I_t to the x-ray beam flux $I_{i2} = I_{i1} + I_{bt}$ entering the DPM without a beam stop (Fig. 5).

For transmission efficiency measurement, firstly, the x-ray reflection spectrum of DPM can be measured by SDD, as shown in Fig. 5. Then DPM was removed, and the primary spectrum can be measured by SDD. The transmission efficiency of DPM for x-rays with energy E can be expressed as

$$\eta_1 = \frac{I_t}{I_{i1}} = \frac{I_2\, e^{-\mu d_1}}{I_1\, e^{-\mu d_2}}, \tag{9}$$

$$\eta_2 = \frac{I_t}{I_{i1} + I_{bt}} = \frac{\eta_1}{1 + \Omega_{bt}/\Omega}, \tag{10}$$

where I_1 is the collected count corresponding to a certain energy E in the primary spectrum without DPM, I_2 is the collected count corresponding to a certain energy E in the reflection spectrum with DPM. d_1 and d_2 are the distances from the entrance and exit of DPM to the SDD, respectively. Ω_{bt} is the solid angle of the beam stop, which is 1.89×10^{-5} sr.

4. Results and discussion

Table 1 shows the parameters of SBPCs. The total slope error of a DPM was calculated by surface profile data, and the details were in Ref. [21]. The total slope error υ_{total} of DPM is including the centerline error δ_1 and the error of the cross-sectional circle δ_2. It can be expressed as

$$\upsilon_{total} = \sqrt{\delta_1^2 + \delta_2^2}. \tag{11}$$

Table 1. Parameters of SBPCs.

Parameters	Pa1	Pa2
Length L (mm)	100	100
Input diameter d_{in} (mm)	1.20	1.20
Output diameter d_{out} (mm)	1.47	1.48
Input focal distance f_1 (mm)	200	–
Output focal distance f_2 (mm)	–	200
Total slope error υ_{total} (μrad·rms)	30.5	31.3

Figure 6 presents a visualization of the simulated x-ray transmission in DPM, illustrating the transmission paths and intensity variations of the x-rays in the x–z coordinate plane. To characterize the DPM, a virtual CCD was employed to capture x-ray intensity data at various z-positions, including photon positions and their corresponding counts.

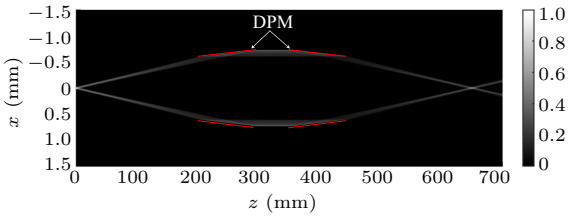


Fig. 6. Visualization of x-ray simulated transmission in DPM.

Figure 7(a) shows simulated intensity distribution of the focal spot of DPM, which is approximately a two-dimensional Gaussian distribution. Figure 7(b) is horizontal normalized intensity distribution marked by the red line in Fig. 7(a). The simulated focal spot size is the full width at half maximum (FHWM) of the Gaussian fitting function (Fig. 7(b)). The simulation program was run 5 times repeatedly. And, the average simulated focal spot size was 104.0 μm with a standard deviation of 0.42. The uncertainty in the simulated focal spot size is mainly caused by the statistical errors in the repeated simulations. Figure 7(c) is experimental image of the focal spot of DPM, and as shown in Fig. 7(d), its normalized intensity distribution is well approximated by a Gaussian function, and the focal spot size is 115.9 μm. The actual compression ratio Ra_a of the DPM for x-ray source is about 0.43. Since the aperture of DPM is too small, it is impossible to directly use atomic force microscopy (AFM) or optical interferometer to accurately measure the inner surface profile of DPM. Therefore, this paper uses the inner-to-outer diameter ratio method to indirectly derive the inner surface profile of DPM. However, this method cannot fully obtain the actual surface slope error, especially the high-frequency components (such as nanoscale roughness or local defects), which leads to deviations between the surface model used in the simulation and the actual DPM. In addition, the preform tube used to draw DPM may have internal inherent defects (such as microcracks and uneven density), and these structural defects cannot be accurately characterized by the inner-to-outer diameter ratio method. These errors, which are not directly measurable, are not included in the simulation model. This results in a slight discrepancy between the experimentally measured focal spot size (115.9 μm) and the simulation result (104.0 μm).

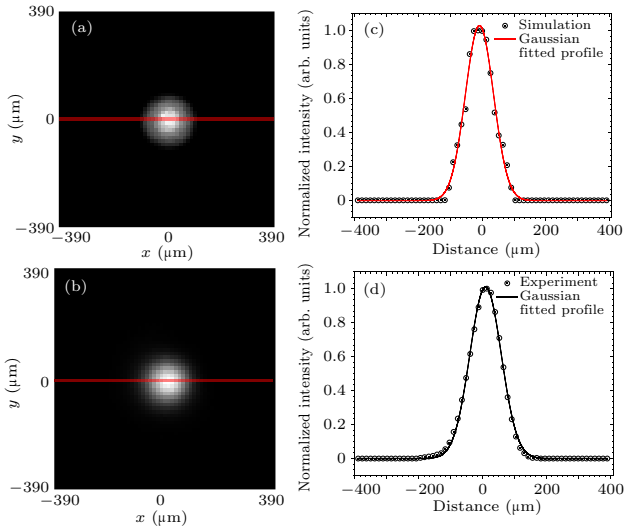


Fig. 7. (a) and (c) Simulated and experimental focal spot images of DPM. (b) and (d) The normalized intensity distributions in the horizontal direction correspond to the red lines in panels (a) and (d), respectively.

The divergence angle of the focusing ring can be obtained by measuring the inner and outer diameters of the focusing ring at different positions. Figure 8 shows the simulated and experimental focusing ring images of DPM. The divergence angle of the focusing ring can be obtained by measuring the inner and outer diameters of the focusing ring at different positions, as shown in Fig. 9. In this study, the simulated maximum and minimum divergence angles are 3.2 mrad and 2.2 mrad, respectively, which closely align with the experimental values of a maximum divergence angle of 3.3 mrad and a minimum of 2.1 mrad. The small deviation between the simulated and experimental divergence angles can be attributed to the same factors as the focal spot size discrepancy. The surface shape error cannot be precisely quantified due to the limited aperture size of the DPM and its complex surface morphology.

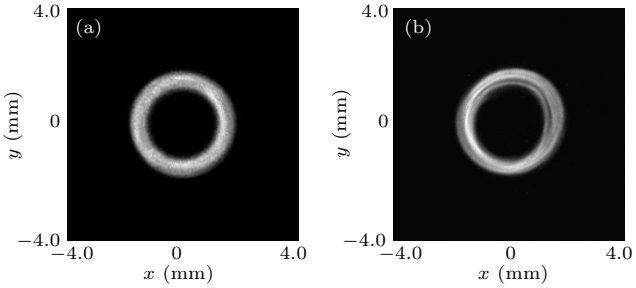


Fig. 8. Simulated and experimental focusing ring images of DPM: (a) simulation, (b) experiment. The inner and outer boundaries of the focusing ring are irregular, which is caused by the shape error of DPM.

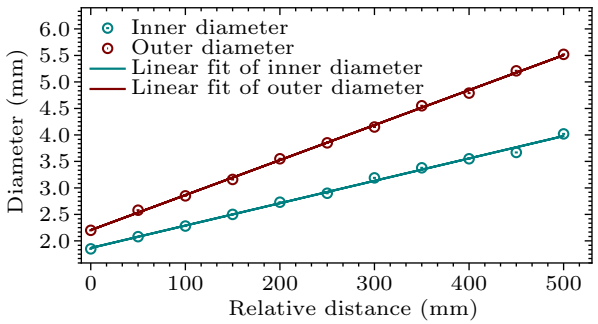


Fig. 9. Divergence angle of the focusing ring. The minimum and maximum divergence angles of the focusing ring are 2.1 mrad and 3.3 mrad, respectively.

Figure 10 shows the comparison of the experimental and simulated transmission efficiencies of DPM, and the simulated transmission efficiency agrees with the experiment. Due to the strong absorption of low-energy x-ray transmission, the transmission efficiency of energy below 10-keV decreases. As the energy of the incident x-ray is greater than 19 keV, the grazing incidence angle θ is gradually larger than the critical angle θ_c of total x-ray reflection, so the transmission efficiency of DPM decreases rapidly. Since θ_c is on the order of milliradians, and the total slope error is on the order of tens of microradians (less than 5% of θ_c), the deviation between the simulated and experimental slope errors is minimal, leading to good agreement in transmission efficiencies.

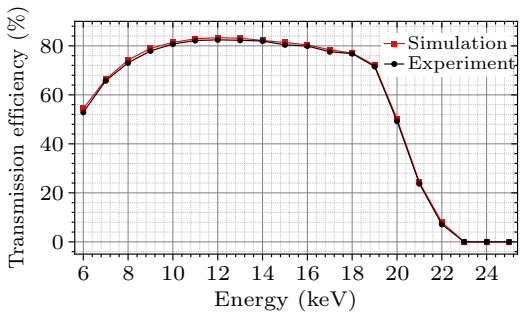


Fig. 10. Comparison of simulated and experimental transmission efficiencies of DPM. The red and black curves are the energy dependence of the simulated and experimental transmission efficiencies, respectively.

5. Conclusion

In this paper, a raytracing method with the mathematical model of the surface shape error was used to simulate the properties of the a DPM (focal spot size, divergence and transmission efficiency). The properties of DPM were characterized, and the experimental results were compared with the simulated ones. The simulated results show good agreement with the experimental data.

We used two approximately identical SBPCs combined into a DPM with a theoretical compression ratio $Ra_t = f_1/f_2 = 1$. In order to obtain a smaller focal spot size, we will focus on the study of DPM ($Ra_t > 1$) composed of different SBPCs in the future.

Acknowledgements

Project supported by project of Beijing Postdoctoral Research Fund (Grant No. 2025-ZZ-86), the National Natural Science Foundation of China (Grant Nos. 12105020 and 12075031), Shenzhen Science and Technology Program (Grant No. KJZD20230923114219040), the Natural Science Youth Foundation of Henan Province, China (Grant No. 242300420637), the Open Fund of Key Laboratory of Beam Technology of the Ministry of Education, Beijing Normal University (Grant No. BEAM2024G02), and the Innovation Cultivation of Beijing Academy of Science and Technology (Grant Nos. 25CB007-01 and 25CB007-02).

References

[1] Sun T, Liu Z, Li Y, Wang G, Zhu G, Ding X, Xu Q, Liu H, Luo P, Pan Q, Lin X and Teng Y 2009 *Spectrochim. Acta B* **64** 1194
[2] Liu H, Liu Z, Sun T, Peng S, Ma Y, Sun W, Li Y, Lin X, Zhao W, Zhao G, Luo P, Pan Q and Ding X 2013 *Nucl. Instrum. Methods Phys. Res. A* **723** 1
[3] Sun T, Liu Z and Ding X 2007 *Chem. Phys. Lett.* **439** 412
[4] Zeng X, Duewer F, Feser M, Huang C, Lyon A, Tkachuk A and Yun W 2008 *Appl. Opt.* **47** 2376
[5] Li F Z, Liu Z G and Sun T X 2016 *Rev. Sci. Instrum.* **87** 093106
[6] Zhu Y, Wang Y, Sun T, Sun X, Zhang X, Liu Z, Li Y and Zhang F 2018 *Appl. Radiat. Isot.* **137** 172
[7] Shao S, Li H, Yuan T, Sun X, Hua L, Liu Z and Sun T 2023 *Chin. Phys. B* **32** 080702
[8] Stern E A, Kalman Z, Lewis A and Lieberman K 1988 *Appl. Opt.* **27** 5135
[9] Bilderback Donald H, Hoffman Stephen A and Thiel Daniel J 1994 *Science* **263** 201
[10] Kuczumow A and Larsson S 1994 *Appl. Opt.* **33** 7928
[11] Huang R and Bilderback D H 2001 *Nucl. Instrum. Meth. A* **467** 978
[12] Lamb J S, Cornaby S, Andresen K, Kwok L, Park H Y, Qiu X Y, Smilgies D M, Bilderback D H and Pollack L 2007 *J. Appl. Crystallogr.* **40** 193
[13] Li Y L, Wang Y B, Lu W E, Kong X D, Han L and Zhao H B 2021 *Chin. Phys. B* **30** 050703
[14] Sirenko A A, Kazimirov A, Cornaby S, Bilderback D H, Neubert B, Brückner P, Scholz F, Shneidman V and Ougazzaden A 2006 *Appl. Phys. Lett.* **89** 181926
[15] Barrea R A, Huang R, Cornaby S, Bilderback D H and Irving T C 2009 *J. Synchrotron Radiat.* **16** 76
[16] Woll A R, Mass J, Bisulca C, Huang R, Bilderback D H, Gruner S and Gao N 2006 *Appl. Phys. A* **83** 235
[17] Huang R and Bilderback D H 2006 *J. Synchrotron Radiat.* **13** 74
[18] Lin X Y, Li Y D, Sun T X and Pan Q L 2010 *Chin. Phys. B* **19** 070205
[19] Hudec R, Valníček B, Svatek L, Landa V and Fiedorowicz H 1988 *Le Journal de Physique Colloques* **49** C1
[20] Jiang B, Liu Z, Sun X, Sun T, Deng B, Li F, Yi L, Yuan M, Zhu Y, Zhang F, Xiao T, Wang J and Tai R 2017 *Opt. Commun.* **398** 91
[21] Shao S, Li H, Tao F, Wang Y, Zhang X, Yuan T, Sun X, Liu Z, Deng B and Sun T 2021 *Nucl. Instrum. Methods Phys. Res. A* **1014** 165735
[22] Takano A, Maehata K, Iyomoto N, Hara T, Mitsuda K, Yamasaki N and Tanaka K 2018 *IEEE Trans. Nucl. Sci.* **65** 758
[23] Zymierska D 1996 *Acta Phys. Pol. A* **89** 347
[24] Li Y D, Lin X Y, Tan Z Y, Sun T X and Liu Z G 2011 *Chin. Phys. B* **20** 040702
[25] See https://physics.nist.gov/PhysRefData/FFast/html/form.html for the "Basic Information" (last accessed April 02, 2025), retrieved
[26] Wang Y, Li Y, Shao S, Zhang X, Li Y, Sun X, Tao F, Deng B and Sun T 2020 *Opt. Commun.* **464** 125544